ACS APPLIED ENERGY MATERIALS

www.acsaem.org

Forum Article

# Rapid Carbonization of Anthracite Coal via Flash Joule Heating for Sodium Ion Storage

Shu Dong, Yali Song, Yongzheng Fang, Guiling Wang, Yinyi Gao, Kai Zhu,* and Dianxue Cao*

Cite This: https://doi.org/10.1021/acsaem.3c02975

Read Online

ACCESS | Metrics & More | Article Recommendations | Supporting Information



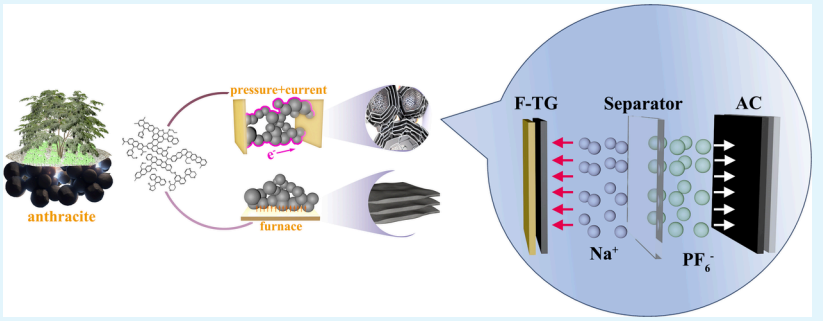


**ABSTRACT:** Anthracite coal holds great promise as a prospective anode material for sodium ion batteries. However, traditional preparation methods suffer from prolonged calcination time and significant energy consumption, impeding high-throughput synthesis and structural control of anthracite coal. To address these challenges, we propose an emerging rapid carburization method for anthracite coal utilizing flash joule heating, which enables the removal of noncarbon components within one second at an ultrafast heating rate. Under a jolt of electricity, the prepared anthracite coal exhibits a turbostratic graphite-encased porous carbon structure with larger interlayer spacing than that achieved through high-temperature furnace annealing. The anthracite coal prepared via flash joule heating demonstrates high reversible capacity (209 mAh $g^{-1}$ at 0.05 A $g^{-1}$) and significantly enhanced rate capability (reaching 115 mAh $g^{-1}$ at 1 A $g^{-1}$), with no capacity decay observed after 500 cycles in a sodium-ion half-cell. These findings highlight the potential of flash joule heating in rapid and efficient synthesis of anthracite coal, offering new possibilities for the development of high-performance anode materials in the next generation of sodium-ion batteries.

**KEYWORDS:** *sodium-ion batteries, anthracite, flash joule heating, rapid carbonization, turbostratic layer*

## 1. INTRODUCTION

The rechargeable secondary battery industry has experienced explosive growth over the past decade. The International Energy Agency (IEA) predicts that the annual production of electric vehicle batteries will reach 6660 GWh by 2030.[1] However, the low natural abundance of lithium resources and their uneven distribution geographically necessitate the search for another lower-cost system to achieve sustainability.[2,3] As a member of the alkali metal group, sodium, with a standard reduction potential of −2.7 V (vs. RHE), is widely distributed in both terrestrial and marine environments.[4] It shares similar energy storage mechanisms with lithium batteries and employs analogous manufacturing processes. Sodium-ion batteries (SIBs) are considered strong candidates for the postlithium era. Various types of anodes are used in SIBs, including traditional carbon materials,[5] sodium alloy anodes,[6−8] metal oxide nanomaterials,[9−11] organic material,[12] and sodium metal anodes.[13] Among these, carbon materials remain the most promising option for commercialization. However, the commercially used anode material in lithium-ion batteries (LIBs), graphite, demonstrates restricted performance in sodium storage, offering a mere 35 mAh $g^{-1}$ of reversible capacity. This underscores the need for special structural characteristics in carbon materials employed for sodium storage, designed to accommodate the larger ionic radius of $Na^+$ (1.02 Å) and the inherent instability of Na−C compounds.[14]

The storage process of sodium ions in carbon materials involves multiple mechanisms. At high voltages, sodium ions are stored between layers through adsorption or intercalation mechanisms. At low voltages (<0.1 V), sodium clusters are formed within closed pores for storage. Throughout these processes, specific requirements exist for the interlayer spacing and morphology of carbon materials. An ideal carbon material structure should possess a moderate specific surface area to

Special Issue: Early Career Forum 2024

Received: November 30, 2023
Revised: December 30, 2023
Accepted: January 2, 2024

support both adsorption and intercalation mechanisms while having appropriate closed pore structures to accommodate and stabilize sodium clusters formed in the low-voltage region. This balanced structure can achieve high energy storage capacity and excellent reversibility, making carbon materials ideal for sodium-ion battery anodes. Therefore, meticulous design of carbon material structures to meet the specific requirements of different voltage regions is crucial for enhancing sodium battery performance.

The anode for sodium batteries is typically derived from the pyrolysis of carbon sources with aromatic topological structures. Common precursors include natural graphite, biomass-derived, resin-based, coal-based, and organic polymers. Compared to the high collection difficulty of biomass materials and the high cost of organics, coal is easily mined and cost-effective. Coal-based materials encompass coal tar pitch, bituminous coal, lignite, and anthracite. Among them, the high degree of metamorphism and low volatile content of anthracite result in a higher carbon yield compared to other precursors. Due to its condensed aromatic ring structure, the changes in anthracite during heating are complex, undergoing processes such as softening, melting, reorganization, and solidification. During this process, carbon layers tend to undergo orderly stacking and graphitization, which is not conducive to sodium ion storage. Increasing the heating rate stands as a potential measure to address this issue. However, the costs linked to attaining rapid heating in a high-temperature furnace are substantial. When subjected to high-temperature furnace heating, the gaseous small molecules generated tend to be swiftly carried away by the flowing protective gas, thereby diminishing the overall yield. Additionally, slow annealing could potentially exacerbate the stacking of carbon layers.

Moreover, the conductivity of carbon materials from direct pyrolysis is unsatisfactory, failing to meet the demands of high-rate charging and discharging. Some studies have reported that introducing an electric field during heating can effectively enhance the material's conductivity.[15,16]

In this study, Joule heating was employed to achieve rapid temperature elevation. Among various Joule heating devices,[17,18] to allow current to pass through the carbon material, we adopted the flash Joule heating (FJH) method reported by Tour's team,[19] which boasts rapid reaction time and high reaction temperatures. Compared to the radiant cooling method of traditional high-temperature furnaces, blackbody radiation can release most of the heat within milliseconds. This ultrafast method can alleviate the carbon layer stacking phenomenon during coal pyrolysis. Under the influence of an electric field, anthracite restructures and stacks into a turbostratic carbon layer, forming a three-dimensional continuous carbon network. Heating methods such as microwave irradiation and spray pyrolysis cannot achieve materials capable of sustaining high current densities, which constitutes a unique advantage of FJH. Fossil fuel use is projected to decline further by 2050 based on the assumption that countries meet their national net-zero emissions pledges. The design of coal-based anode structures can promote its application in energy conversion, paving a new way for the high-value transformation of traditional fossil fuels.

## 2. MATERIALS AND METHODS

**2.1. Materials.** The anthracite was obtained from Heilongjiang Huasheng Graphite Co., Ltd. The Polyvinylidene fluoride (PVDF), Super-P, glass microfiber filters (Whatman GF/D), *N*-methyl pyrrolidone (NMP) and active carbon were all purchased from Guangdong Canrd New Energy Technology Co., Ltd. The 1.0 M sodium hexafluorophosphate ($NaPF_6$) in dimethoxyethane (DME) and 1.0 M $NaPF_6$ in ethylene carbonate: ethyl methyl carbonate: dimethyl carbonate (EC: DMC: EMC = 1:1:1 Vol.%) were purchased from Dodochem Co., Ltd.

**2.2. Anthracite Ash Removal.** The anthracite was crushed, sieved, and then reacted with KOH solution in a high-pressure reactor at 320 °C for 3 h. Afterward, it was washed with water to remove the alkali, treated with hydrochloric acid to remove inorganic salts, and then washed and dried. The resulting product has a carbon content of over 99%. The anthracite powder obtained was processed for carbonization using two separate techniques: first, heating in a tube furnace (GSL-1800X-S, Shenzhen Kejing Star Technology Company) sintered at 800 °C for 2 h with a heating rate of 10 °C per minute, and second, employing a flash Joule heating reactor. The mass of powder utilized for each reaction was 100 mg.

**2.3. Material Characterization.** The transmission electron microscope (JEOL, JEM-2100) and atomic force microscope (Bruker, Dimension Icon) were employed for observing F-rGO microstructures. The nitrogen adsorption−desorption isotherms were obtained using the Micromeritics TriStar II instrument. The sample mass of 100 mg was used for testing, with a degassing temperature of 200 °C and an 8 h degassing period before conducting the tests. X-ray diffraction (XRD) using Bruker D8 type covered the 5−90° range with filtered Cu K$\alpha$ radiation ($\lambda$ = 1.5418 Å). Raman spectroscopy was conducted with the Horiba-Jobin-Yvon LabRAM HR800c spectrometer. Surface analysis utilized the Thermofisher Escalab Xi+ for XPS experiments, employing Al K$\alpha$ radiation (1486.6 eV), with a 500 $\mu$m light spot size. High-resolution spectra are obtained with a 30 eV pass energy and 0.05 eV step size, followed by peak fitting for analysis. The electrical conductivity of the electrode material was determined using a four-point probe instrument (RM 3000+, Jandel Engineering, U.K.).

**2.4. Electrochemical Measurements.** The prepared electrode material, PVDF (polyvinylidene fluoride), and Super P were mixed in NMP with an 8:1:1 mass ratio, achieving a uniform slurry through magnetic stirring. This mixture was spread onto Cu foil and dried in a vacuum at 120 °C for 6 h. Using this, FA3/Na half cells were constructed in coin-type cells (CR2032). The electrode of FA3 and a sodium sheet were divided by a glass microfiber filters (16 mm). The electrolyte used was a mixture of 1 M $NaPF_6$ in DME. To make a comparison, batteries employing an ester-based electrolyte are also tested, containing 1 M $NaPF_6$ in EC:DMC:EMC = 1:1:1 Vol.%. Electrochemical tests on the half-cells included cyclic voltammetry (CV, range 0−3 V *vs* $Na^+/Na$, sweep rate between 0.2−5 mV $s^{-1}$) and electrochemical impedance spectroscopy (EIS, frequency from 100 kHz to 0.01 Hz, amplitude 10 mV). These tests were conducted using an IVIUM-N-STAT multichannel workstation in a controlled environment (25 ± 2 °C, Ivium Technologies B.V.). The impedance results were fitted with Zview software. Galvanostatic charge and discharge (GCD) cycling of the half-cells was done on a Neware battery tester (CT-3008W). The sodium-ion capacitive batteries with ether-based electrolytes were assembled using a similar methodology. The voltage testing range for AC/Na was set be between 3 and 4 V, while for AC//FA3, the voltage testing range spanned from 1 to 4 V.

## 3. RESULTS AND DISCUSSION

The circuitry and composition of the FJH reactor are illustrated in Figure S1 of the Supporting Information. The high-purity anthracite powder, obtained after sieving, is introduced into a glass reactor with openings at both ends. By adjusting the spring pressure at both ends, the initial resistance of each sample is consistently maintained. The charging voltage of the parallel plate capacitor is precisely set to 150 V using a knob, and then the insulate-gate bipolar (IGBT) switch is used to achieve instantaneous discharge of the capacitors.[19] The resulting products from 1, 3, and 5 times


https://doi.org/10.1021/acsaem.3c02975
ACS Appl. Energy Mater. XXXX, XXX, XXX−XXX

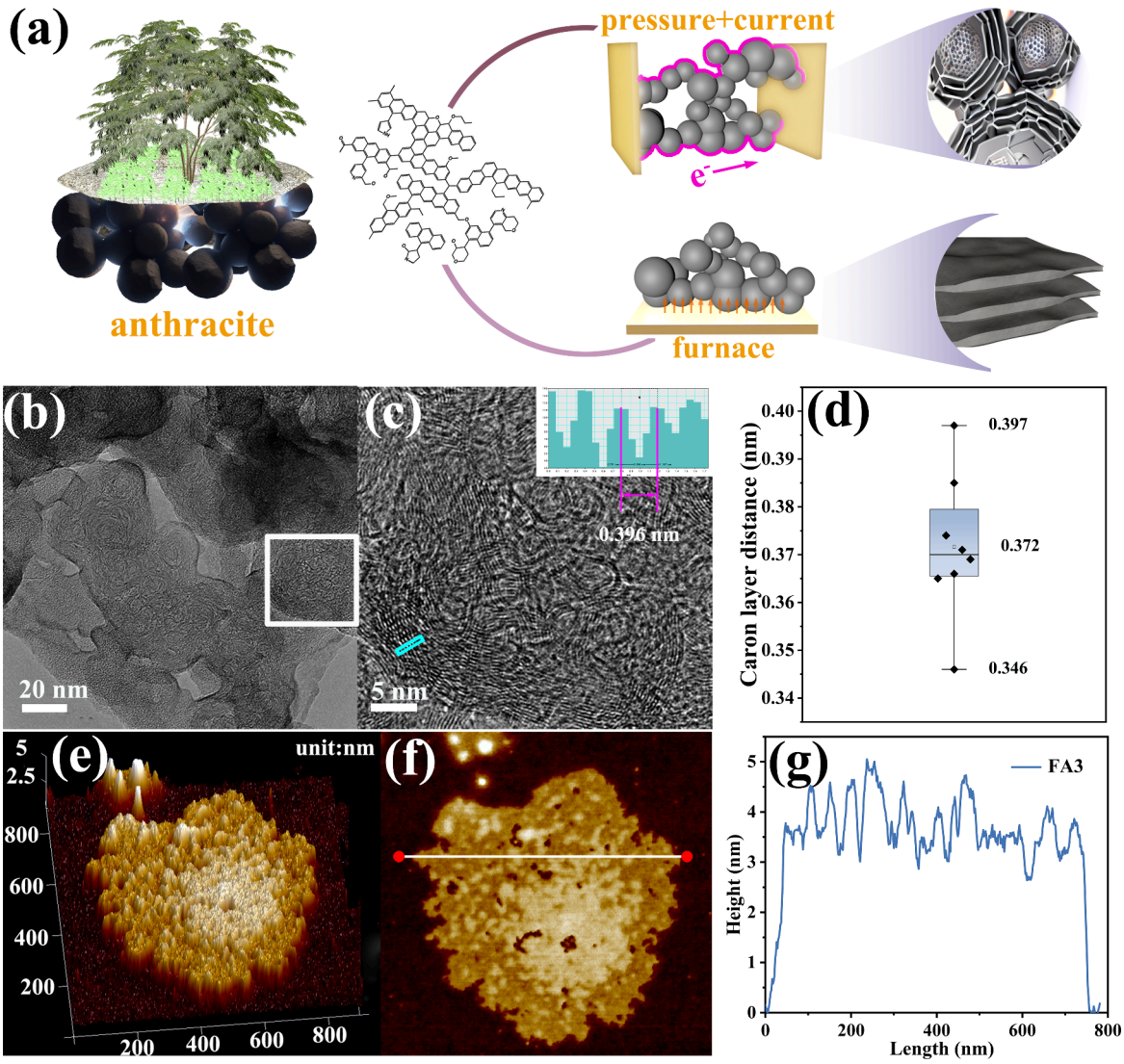


**Figure 1.** Schematic of the FJH process and product morphologies. (a) Scheme of the reaction mechanisms in FJH process for anthracite. (b–d) TEM images of FA3 and boxplots of interlayer spacing measurements in selected regions. (e–g) AFM images of FA3.

of discharges are labeled as FA1, FA3, and FA5, respectively. Bright light is observed during the FJH reaction, indicating the occurrence of the Joule heating effect, with the light lasting less than 0.1 s. The heat generated during the reaction is released in the form of blackbody radiation.[18] With an increasing number of discharges, the brightness of the reaction gradually diminishes.

The microstructure of the three FJH reaction products is shown in Figures S2 and S3. The initial anthracite coal exhibits an agglomerated structure. After one FJH reaction, short, curled carbon layers start to appear in FA1, but the majority of the region remains amorphous as determined by transmission electron microscopy (TEM). While the FJH is performed in triplicate, high-resolution TEM reveals an increase in the turbostructure of carbon layers (Figures 1b,c). These carbon layers lack a specific orientation, interconnect with each other, and locally form enclosed pores. Measurements of the carbon layer spacing at multiple positions (Figures 1d and S4) show a distribution ranging from 3.46 to3.97 Å, overall greater than the interlayer spacing in graphite. Furthermore, the atomic force microscope (AFM) images also depict the presence of the turbine-like structure (Figure 1e–g). After five FJH reactions, TEM images of the product display a structure where outer ordered turbo carbon layers encase inner curled carbon layers (Figure S5). The crystallinity of the outer carbon layers significantly improves compared to FA1 and FA3, and the thickness of graphitized layers also noticeably increases. The carbon layer spacing in FA5 (3.44 Å) remains greater than the typical Bernal stacked graphite interlayer distance of 3.35 Å, attributed to the rapid heating and cooling characteristics of FJH.[19,20] We prepared Anthracite directly pyrolyzed in a tube furnace at 800 °C (TF-800). SEM images (Figure S2) indicate that FA exhibits a higher quantity of pores compared to TF-800. The isothermal adsorption–desorption curve (Figure S6) of FA exhibits a Type H2 hysteresis loop among the Type IV isotherms, thereby affirming its porous nature. The calculated desorption average pore diameter using the BJH (Barrett–Joyner–Halenda) method is 7.09 nm.[21] In contrast, the surface area of TF-800 is lower than that of FA3, and displays an uneven pore size distribution.

The degree of ordering of the product is characterized by X-ray diffraction (XRD), and it is observed that with an increasing number of FJH reaction cycles, the (002) peak becomes sharper, indicating the formation of more ordered


https://doi.org/10.1021/acsaem.3c02975
ACS Appl. Energy Mater. XXXX, XXX, XXX–XXX

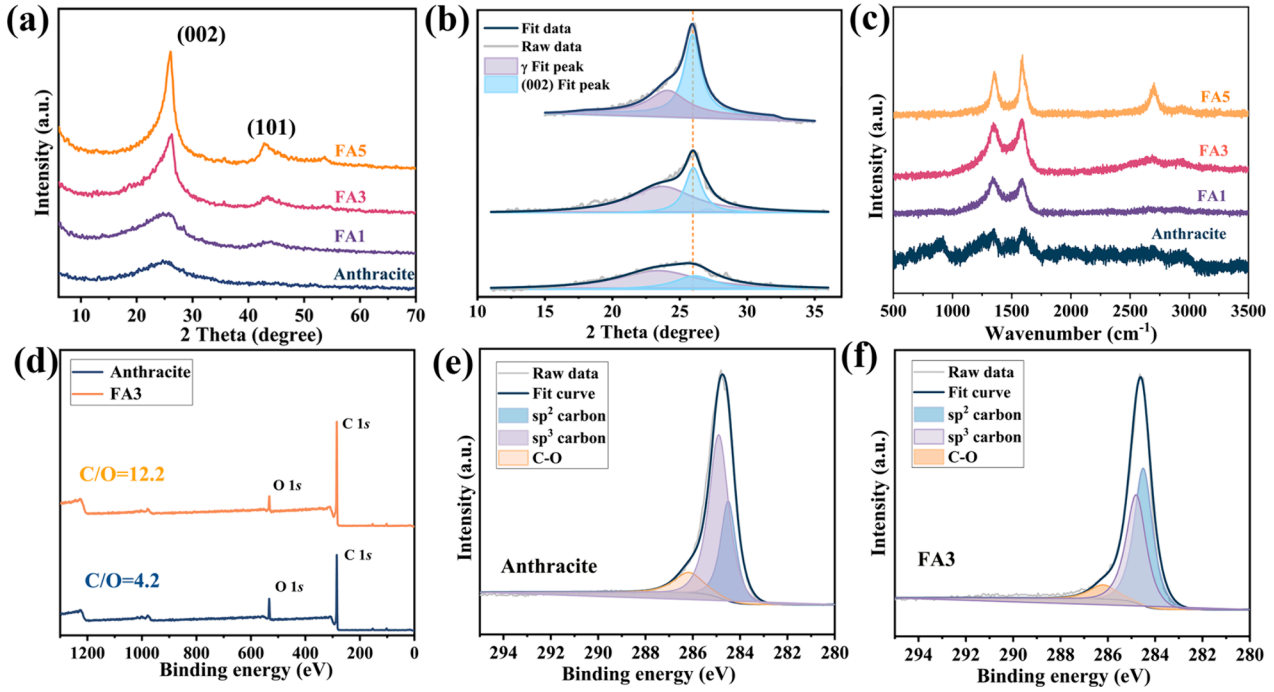


**Figure 2.** Phase characterization of FJH products. (a, b) XRD and curve fitting of two Lorentzian peaks for flashed anthracite in the $2\theta$ range of 10−35°. (c) Raman spectra of the products. (d−f) XPS spectra and peak fitting for the initial anthracite and FA3.

microcrystalline and graphite domains. Asymmetrical peak shapes, broad tails, and an upward tilt in the small-angle diffraction patterns suggest the coexistence of graphitic and amorphous domains (Figure 2a). The peak corresponding to the (002) plane (with an interlayer spacing of 3.42 Å at a fixed diffraction angle of 26.02°) is determined, and a Lorenzian fit provides the (002) peak and the $\gamma$ peak (Figure 2b). The proportion of the (002) peak area reflects the degree of graphitic stacking, with the calculated results presented in Table 1. According to the Scherrer formula (eq 1), the lateral

**Table 1**

| sample | $A_{(002)}/A_{(\gamma)}+A_{(002)}$ | $\gamma$ | $L_a$ (nm) | $L_c$ (nm) |
|---|---|---|---|---|
| FA1 | 0.27 | 24.08° | / | 1.3 |
| FA3 | 0.30 | 22.67° | 3.5 | 2.1 |
| FA5 | 0.60 | 22.38° | 4.1 | 3.0 |

size ($L_a$) of carbon layers and the stacking height ($L_c$) of aromatic layers are calculated. It can be observed that, as the number of discharge cycles increases, the proportion of graphitic stacking increases, resulting in larger stack thickness and layer dimensions, consistent with the observations from TEM. These results indicate a clear positive correlation between the number of FJH reaction cycles and the degree of graphitization of the product.[22]

$$D_{(hkl)} = \frac{K\lambda}{\beta\cos(\theta)} \quad (1)$$

in which $L_a = D_{(101)}$, $L_C = D_{(002)}$, $K$ is the shape factor which is most commonly taken as 0.89, $\lambda$ is wavelength of X-ray (1.54 Å for Cu target), and $\beta$ is the half width of (hkl) peak.

Based on the above analysis, we further examined the structural evolution of anthracite coal during the FJH process using Raman spectroscopy. Figure 2c presents the Raman spectra of different FJH reaction products. The initial anthracite coal sample exhibited a strong fluorescence effect due to the presence of organic matter, resulting in disordered Raman peaks. After FJH, two sets of typical D peaks (1350 $cm^{-1}$) and G peaks (1580 $cm^{-1}$) appeared in the spectra, corresponding to the in-plane stretching modes of carbon atoms, and their intensity is closely related to the crystallinity of carbon materials. The $I_D/I_G$ intensity ratio is typically used to assess the degree of disorder in a sample.[23] The $I_D/I_G$ for FA1 is 0.98, while as the reaction progresses, the values for FA3 and FA5 decrease to 0.94 and 0.81, respectively. With the prolonged duration of FJH reactions, the G peak intensity increases, and the peak width narrows, indicating an enhanced level of order.[24] This is consistent with the XRD results and provides strong evidence that the FJH reaction can promote the crystallinity of anthracite coal under low-energy consume.

After the FJH reaction, anthracite coal undergoes a polymerization reaction, resulting in an increased degree of aromatization. X-ray photoelectron spectroscopy (XPS) results reveal an increase in components related to carbon and a decrease in components related to oxygen functional groups. The C 1s peak can be deconvoluted into three peaks corresponding to the binding energies of $SP^2$ C, $SP^3$ C, and C−O, located at 284.5, 284.8, and 286.2 eV, respectively.[25] After three FJH reactions, the proportion of $SP^2$ C increases from 28% to 53%, while the proportion of $SP^3$ C decreases from 60% to 42%, indicating an enhanced degree of aromatization in the product. The increase in the number of continuous aromatic rings in the FJH product enhances electronic conjugation and conductivity, thereby improving electrical conductivity.

Based on the above analysis, it can be inferred that as the reaction time of FJH increases, anthracite coal, which primarily possesses an amorphous structure, gradually transforms into a structure surrounded by ordered carbon layers of a certain thickness. It is reasonable to assume that following the discharge of the capacitor, the material experiences a relatively


https://doi.org/10.1021/acsaem.3c02975
ACS Appl. Energy Mater. XXXX, XXX, XXX−XXX

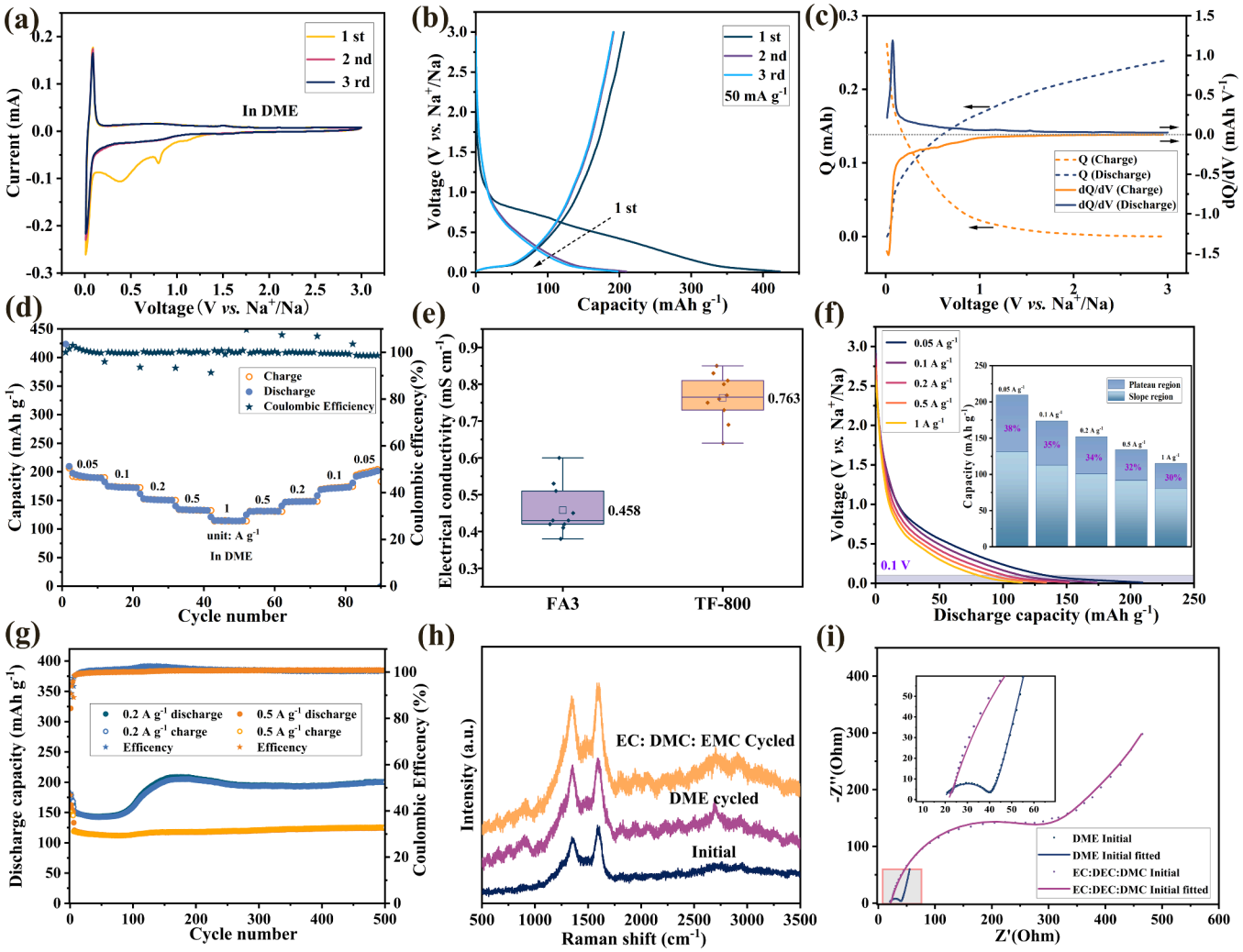


**Figure 3.** Electrochemical performance of FA3 in Na-ion half-cell using ether-based electrolyte. (a) The initial three CV curves and (b) GCD curves at 0.05 A $g^{-1}$ of FA3 at a voltage of 0.01−3 V. (c) Differential capacity analysis. (d) Rate performance of FA3 at current densities in the range of 0.05−1 A $g^{-1}$. (e) The thin film conductivity of FA3 and TF800. (f) Discharge curves from 0.05 A $g^{-1}$ to 1 A $g^{-1}$. (g) Cycling performances at 0.2 A $g^{-1}$ and 0.5 A $g^{-1}$ for FA3 in DME electrolyte. (h) Ex-situ Raman curves. (i) EIS plots and fitting curves of FA3 in DME electrolyte and EC/DEC/DME electrolyte.

high bias voltage at both ends, causing a significant influx of electrons into the initial anthracite. Electrons predominantly follow along conductive pathways, specifically interconnecting large aromatic layers. According to Joule's law, the resistance surrounding these conductive pathways generates a substantial amount of Joule heat as current passes through. The rigid, conductive portions retain their interconnected structure, with atoms maintaining a locally favorable arrangement and exhibiting very low mobility. The joule heat leads to the rupture of unstable $SP^3$ bonds and bridge bonds. The hydrogen atoms in anthracite coal facilitate its transformation into a mobile carbon source.[26] These carbon atoms aggregate and aromatize under the influence of the current, and the strong $\pi-\pi$ interactions between aromatic molecules lead to the stacking of outer carbon layers, forming a graphite-like structure.[20,27] Under the influence of Joule heating, open carbon edges are fused together, connecting these edges to form enclosed pores.[28] With extended FJH treatment, thin layers begin to accumulate layer by layer in a graphite-like form, enclosing core particles. This structure is conducive to electron transport, enhancing the diffusion rate of electrons within the electrode.[29] However, excessively thick graphite layers can reduce the material's porosity and decrease the interlayer spacing, which is unfavorable for sodium storage. In comparison to traditional sintering methods, the rapid heating of the FJH approach preserves the curled structures within anthracite coal, while the fast cooling maintains the interlayer spacing slightly larger than that of graphite layers and preserves the turbo-structure.[30]

We selected FA3 with a moderate carbon layer thickness and closed pores as the anode for the sodium-ion half-cell. As shown in Figure 3a, the reduction peaks at 0.8 and 0.4 V in the first-cycle reduction curve represent the decomposition of the ether-based electrolyte at the electrode surface, forming the SEI (solid electrolyte interface) film, which is also the cause of the initial capacity loss in the charge−discharge curves (Figure 3b). These peaks disappear in subsequent cycles, indicating that the SEI film is primarily formed during the first discharge. In later reduction scans, broad peaks appear in the CV curves, corresponding to the sloping region between 1.5−0.1 V in the charge−discharge curves. When the sodiation potential drops to 0.1 V, distinct reduction peaks begin to appear in the CV


https://doi.org/10.1021/acsaem.3c02975
ACS Appl. Energy Mater. XXXX, XXX, XXX−XXX

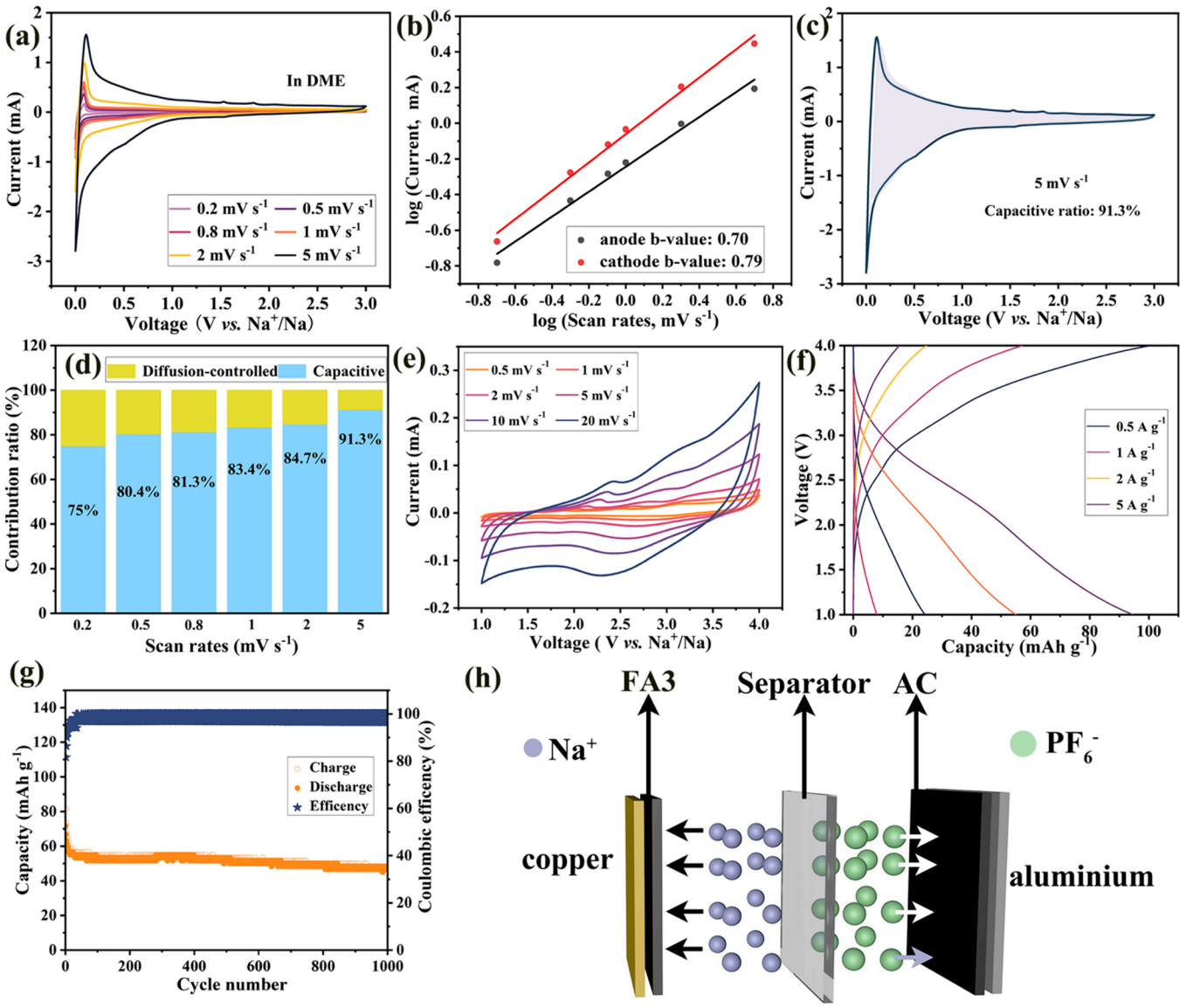


**Figure 4.** (a) CV curves of FA in DME electrolyte at different current densities, and (b–d) the capacitance ratio analysis of FA3. (e) CV curves, (f) GCD curves, (g) cycling performance, and (h) assembly schematic diagram of FA3//AC SICs.

curve, corresponding to the discharge plateau in the charge–discharge curves, which is different from the shuttle-shaped CV curves of many pure carbon-based anodes. The sharp redox peaks of the CV curve suggest that $Na^+$ does not merely undergo simple adsorption on the FA3 surface but also involves intercalation and deposition.

To better understand the changes during the discharge process, a differential capacity analysis was performed (Figure 3c), where the slope of the $dQ/dV$ starts to steepen around 1 V, indicating the start of a phase transformation corresponding to the formation of Na–C compounds, benefiting from the wide interlayer spacing of FA3 that allows the entry of $Na^+$ between the carbon layers. The differential capacitance curve has a steep diagonal line between 0.1–0.01 V, with an upturned peak at the tail, representing the formation of quasi-sodium metal clusters. This behavior is related to the presence of pores in FA3. According to the GCD (galvanostatic charge/discharge) results, FA3 shows a reversible capacity of 209 mAh $g^{-1}$ at a current of 0.05 A $g^{-1}$, and it can deliver reversible capacities of 174, 152, 134, and 115 mAh $g^{-1}$ at current densities of 0.1, 0.2, 0.5, and 1 A $g^{-1}$, respectively (Figure 3d). The excellent rate performance is attributed to the high electronic conductivity of FA3, with an average conductivity of 0.458 mS $cm^{-1}$ (Figure 3e). The impact of current change on capacity is mainly below 1.5 V; with the test current increasing from 0.05 A $g^{-1}$ to 1 A $g^{-1}$, the proportion of plateau capacity decreases from 38% to 30% (Figure 3f), indicating that the pore deposition behavior of sodium is more significantly affected by current changes. After 500 cycles at 0.2 A $g^{-1}$ and 0.5 A $g^{-1}$, there is no capacity decay observed in the half-cell, and after the formation of a stable SEI (within 10 cycles), the Coulombic efficiency of each charge–discharge cycle remains above 99% (Figure 3g), proving that there is no further decomposition of the electrolyte at the stable SEI interface and no significant damage to the material resulting in new irreversible capacity. Whereas TF-800 shows a reversible capacity of only 103 mAh $g^{-1}$ at 0.2 A $g^{-1}$, decreasing to 68 after 500 cycles (Figure S7). The performance of the coal-based anode prepared by the Flash Joule Heating method also exhibits certain advantages compared to other heating methods


https://doi.org/10.1021/acsaem.3c02975
ACS Appl. Energy Mater. XXXX, XXX, XXX–XXX

for coal-based anode preparation (Table S1).[31−35] Such long cycle life is mainly due to the wide interlayer spacing of the outer carbon layer and the carbon mesh structure formed through Joule heat welding, which can reduce strain during cycling.

Compared with ether-based electrolyte, the performance of FA3 in ester-based electrolytes is quite different (Figure S8). The formation of SEI causes a larger irreversible capacity, and the rate performance in ester-based electrolytes is unsatisfactory, with a discharge capacity of 54 mAh $g^{-1}$ at 1 A $g^{-1}$, which is only 35% of the capacity (152 mAh $g^{-1}$) at 0.05 $g^{-1}$. The SEI film formed in the ester-based electrolyte requires stabilization after 20 GCD cycles and exhibits large capacity fluctuations during cycling, indicating the continuous formation and consumption of $Na^+$ by the newly formed SEI film. As shown in Figure 3h, the presence of the 2D peak in the ex-situ Raman test proves that FA3 is able to maintain its original structure in the DME electrolyte. Although there are approximately similar Ohmic impedances, the charge transfer resistance of sodium ions in the ester-based electrolyte is as high as 229 Ω, which is 14.3 times greater than the corresponding value in the ether-based electrolyte (which is 16 Ω). This indicates that sodium ions are more readily stored in the ether-based electrolyte (Figure 3i).

We analyzed the electrochemical behavior of FA3 electrodes using cyclic voltammetry (CV) curves obtained at different scan rates, as depicted in Figure 4a,b. The peak current ($i$) and scanrate ($v$) obeyed eq 2:

$$i = av^b \tag{2}$$

where $a$ and $b$ are fitting parameters, and the value of $b$ ranges from 0.5 to 1.0. When $b$ approaches 1, charge storage in the cell is mainly controlled by capacitive behavior. When $b$ nears 0.5, it is principally governed by semilinear diffusion processes.[36] The $b$ value was calculated from the linear plot of log($i$) versus log($v$), yielding values of 0.79 for the cathode and 0.7 for the anode. These results indicate that sodium storage in the FA3 electrodes is influenced concurrently by capacitive and battery-type behaviors. Equation 3 was also employed to analyze the proportion of capacitive behavior and diffusion processes:

$$i(\mathrm{V}) = k_c v + k_b v^{1/2} \tag{3}$$

where $i$ (V) is the current at a given voltage, and $v$ denotes the scan rate. The terms $k_c v$ and $k_b v^{1/2}$ represent the capacitance behavior and diffusion process, respectively. The ratios of the capacitive behavior increased from 75% to 91.3% as the scan rate increased (Figure 4c,d). In order to verify the potential applications of FA3, we assembled sodium ion capacitors (SICs) using activated carbon (AC) as the cathode and FA3 as the anode. The CV curves of AC exhibited typical rectangular shapes, representing the adsorption behavior of anions in the 1−4 V voltage window (Figure S9). The overall reaction mechanism of the cell is depicted in Figure 4h. We adjusted the mass ratios of FA3 to AC to 1:1, 1:3, and 1:6. The SIC with a mass ratio of 1:3 demonstrated the most regular rectangular curve, and the shape did not change obviously at different sweep rates, indicating domination of capacitive behavior (Figures 4e and S10). The SIC show specific capacities of 95, 55.1, 25.2, and 9.5 mAh $g^{-1}$ at the current densities of 0.5, 1, 2, and 5 A $g^{-1}$, respectively (Figure 4f). After 1000 cycles of GCD at 1A $g^{-1}$, the retained reversible capacity is 46 mAh $g^{-1}$.

## 4. CONCLUSIONS

In conclusion, the series of experiments conducted using the FJH reactor have successfully demonstrated the progressive transformation of anthracite coal into advanced carbon materials with enhanced crystallinity and structural order, as a result of repeated FJH discharge cycles. The results unequivocally show that with an increase in the number of FJH cycles, there is a notable improvement in the graphitic ordering of the carbon layers. Electrochemically, the FA3 sample, with its moderate carbon layer thickness and closed pores, emerged as a superior anode material for Na-ion half-cell batteries, exhibiting high reversible capacity, excellent cycling stability, and high Coulombic efficiency. These electrochemical properties can be largely attributed to the widened interlayer spacing that facilitates $Na^+$ intercalation and the stable SEI layer formed during the initial cycle, which endures without significant degradation or electrolyte decomposition over extensive cycling. Moreover, the study reveals that the rapid heating and cooling intrinsic to the FJH process preserve essential structural features of the anthracite, which are critical for achieving long cycle life and high capacity in battery applications. Overall, the findings of this study not only contribute to a deeper understanding of the effects of FJH processing on anthracite coal but also underscore the importance of tailored structural design in the development of anode materials for sodium-ion batteries. This work lays a foundation for future research on the optimization of coal-based anodes and points toward the possibility of using similar processes to improve the electrochemical performance of other carbonaceous materials.

## ■ ASSOCIATED CONTENT

### Supporting Information

The Supporting Information is available free of charge at https://pubs.acs.org/doi/10.1021/acsaem.3c02975.

Digital photographs of the FJH reactor; SEM image of FA3 and TF-800; TEM images of FA1, FA3, and FA5; BET results; electrochemical performance of TF-800 and ester-based half-cell; comparative analysis with related works; and electrochemical performance of AC and SICs with different mass ratios of FA3:AC (PDF)

## ■ AUTHOR INFORMATION


### Corresponding Authors

**Kai Zhu** − *College of Material Science and Chemical Engineering, Harbin Engineering University, Harbin 150001, P. R. China;* orcid.org/0000-0002-9451-0890; Email: kzhu@hrbeu.edu.cn

**Dianxue Cao** − *College of Material Science and Chemical Engineering, Harbin Engineering University, Harbin 150001, P. R. China;* orcid.org/0000-0001-9138-7295; Email: caodianxue@hrbeu.edu.cn

### Authors

**Shu Dong** − *College of Material Science and Chemical Engineering, Harbin Engineering University, Harbin 150001, P. R. China*




https://doi.org/10.1021/acsaem.3c02975
ACS Appl. Energy Mater. XXXX, XXX, XXX−XXX

**Yali Song** − *College of Material Science and Chemical Engineering, Harbin Engineering University, Harbin 150001, P. R. China*

**Yongzheng Fang** − *School of Chemical Engineering, Zhengzhou University, Zhengzhou 450001 Henan, P. R. China*

**Guiling Wang** − *College of Material Science and Chemical Engineering, Harbin Engineering University, Harbin 150001, P. R. China;* orcid.org/0000-0003-2842-2355

**Yinyi Gao** − *College of Material Science and Chemical Engineering, Harbin Engineering University, Harbin 150001, P. R. China*

Complete contact information is available at: https://pubs.acs.org/10.1021/acsaem.3c02975

## Author Contributions

S.D.: Conceptualization, data curation, and investigation. Y.S.: Data curation, writing-original draft. Y.F.: Data curation and investigation. G.W.: Supervision. Y.G.: Investigation. K.Z.: Investigation and supervision. D.C.: Conceptualization and supervision. The manuscript was written through contributions of all authors. All authors have given approval to the final version of the manuscript.

## Funding

This work was supported by the Student Research and Innovation Fund of the China Fundamental Research Funds for the Central Universities [3072022JIP1003], and Heilongjiang Province Key R&D Program (GA22A014).

## Notes

The authors declare no competing financial interest.

## REFERENCES

(1) *Net Zero by 2050 Data Explorer—Data Tools*; IEA, https://www.iea.org/data-and-statistics/data-tools/net-zero-by-2050-data-explorer (accessed 2023−10−24).

(2) He, X.; Kaur, S.; Kostecki, R. Mining Lithium from Seawater. *Joule* **2020**, *4* (7), 1357−1358.

(3) Gong, Z.; Li, Z.; Wang, P.; Jiang, K.; Bai, Z.; Zhu, K.; Yan, J.; Ye, K.; Wang, G.; Cao, D.; Chen, G. Conductive Framework-Stabilized Zn-Metal Anodes for High-Performance Zn-Ion Batteries and Capacitors. *Energy Mater. Adv.* **2023**, *4*, 0035.

(4) Vaalma, C.; Buchholz, D.; Weil, M.; Passerini, S. A Cost and Resource Analysis of Sodium-Ion Batteries. *Nat. Rev. Mater.* **2018**, *3* (4), 1−11.

(5) Li, Q.; Liu, X.; Tao, Y.; Huang, J.; Zhang, J.; Yang, C.; Zhang, Y.; Zhang, S.; Jia, Y.; Lin, Q.; Xiang, Y.; Cheng, J.; Lv, W.; Kang, F.; Yang, Y.; Yang, Q.-H. Sieving Carbons Promise Practical Anodes with Extensible Low-Potential Plateaus for Sodium Batteries. *Natl. Sci. Rev.* **2022**, *9* (8), nwac084.

(6) Guo, Z.; Qian, G.; Wang, C.; Zhang, G.; Yin, R.; Liu, W.-D.; Liu, R.; Chen, Y. Progress in Electrode Materials for the Industrialization of Sodium-Ion Batteries. *Prog. Nat. Sci.: Mater. Int.* **2023**, *33* (1), 1−7.

(7) Ye, S.; Wang, L.; Liu, F.; Shi, P.; Yu, Y. Integration of Homogeneous and Heterogeneous Nucleation Growth via 3D Alloy Framework for Stable Na/K Metal Anode. *eScience* **2021**, *1* (1), 75−82.

(8) Li, Y.; Lai, X.; Qu, J.; Lai, Q.; Yi, T. Research Progress in Regulation Strategies of High-Performance Antimony-Based Anode Materials for Sodium Ion Batteries. *Acta Phys. -Chim. Sin.* **2022**, *38* (11), 2204049.

(9) Dong, G.; Li, L.; Zhu, K.; Yan, J.; Wang, G.; Cao, D. Solvent Induced Activation Reaction of MoS2 Nanosheets within Nitrogen/Sulfur-Codoped Carbon Network Boosting Sodium Ion Storage. *Small* **2023**, *19* (26), 2208291.

(10) Dong, G.; Yu, H.; Li, L.; Zhang, R.; Yang, X.; Zhu, K.; Wang, G.; Cao, D. Surface Engineering of Core-Shell MoS2@N-Doped Carbon Spheres as Stable and Ultra-Long Lifetime Anode for Sodium-Ion Batteries. *J. Colloid Interface Sci.* **2023**, *647*, 395−405.

(11) Tang, J.; Peng, X.; Lin, T.; Huang, X.; Luo, B.; Wang, L. Confining Ultrafine Tin Monophosphide in Ti3C2Tx Interlayers for Rapid and Stable Sodium Ion Storage. *eScience* **2021**, *1* (2), 203−211.

(12) Zhao, L.; Zhao, J.; Hu, Y.; Li, H.; Zhou, Z.; Armand, M.; Chen, L. Disodium Terephthalate ($Na_2C_8H_4O_4$) as High Performance Anode Material for Low-Cost Room-Temperature Sodium-Ion Battery. *Adv. Energy Mater.* **2012**, *2* (8), 962−965.

(13) Tian, Y.; Sun, Y.; Hannah, D. C.; Xiao, Y.; Liu, H.; Chapman, K. W.; Bo, S.-H.; Ceder, G. Reactivity-Guided Interface Design in Na Metal Solid-State Batteries. *Joule* **2019**, *3* (4), 1037−1050.

(14) Zhang, W.; Zhang, F.; Ming, F.; Alshareef, H. N. Sodium-Ion Battery Anodes: Status and Future Trends. *EnergyChem.* **2019**, *1* (2), 100012.

(15) Liu, Y.; Li, P.; Wang, F.; Fang, W.; Xu, Z.; Gao, W.; Gao, C. Rapid Roll-to-Roll Production of Graphene Films Using Intensive Joule Heating. *Carbon* **2019**, *155*, 462−468.

(16) Upama, S.; Mikhalchan, A.; Arévalo, L.; Rana, M.; Pendashteh, A.; Green, M. J.; Vilatela, J. J. Processing of Composite Electrodes of Carbon Nanotube Fabrics and Inorganic Matrices via Rapid Joule Heating. *ACS Appl. Mater. Interfaces* **2023**, *15* (4), 5590−5599.

(17) Senneca, O.; Urciuolo, M.; Chirone, R.; Cumbo, D. An Experimental Study of Fragmentation of Coals during Fast Pyrolysis at High Temperature and Pressure. *Fuel* **2011**, *90* (9), 2931−2938.

(18) Wang, C.; Zhong, W.; Ping, W.; Lin, Z.; Wang, R.; Dai, J.; Guo, M.; Xiong, W.; Zhao, J.; Hu, L. Rapid Synthesis and Sintering of Metals from Powders. *Adv. Sci.* **2021**, *8* (12), 2004229.

(19) Luong, D. X.; Bets, K. V.; Algozeeb, W. A.; Stanford, M. G.; Kittrell, C.; Chen, W.; Salvatierra, R. V.; Ren, M.; McHugh, E. A.; Advincula, P. A.; Wang, Z.; Bhatt, M.; Guo, H.; Mancevski, V.; Shahsavari, R.; Yakobson, B. I.; Tour, J. M. Gram-Scale Bottom-up Flash Graphene Synthesis. *Nature* **2020**, *577* (7792), 647−651.

(20) Stanford, M. G.; Bets, K. V.; Luong, D. X.; Advincula, P. A.; Chen, W.; Li, J. T.; Wang, Z.; McHugh, E. A.; Algozeeb, W. A.; Yakobson, B. I.; Tour, J. M. Flash Graphene Morphologies. *ACS Nano* **2020**, *14* (10), 13691−13699.

(21) Zeng, C.; Duan, C.; Guo, Z.; Liu, Z.; Dou, S.; Yuan, Q.; Liu, P.; Zhang, J.; Luo, J.; Liu, W.; Zhang, J.; Chen, Y.; Hu, W. Ultrafastly Activated Needle Coke as Electrode Material for Supercapacitors. *Prog. Nat. Sci.: Mater. Int.* **2022**, *32* (6), 786−792.

(22) Chen, H.; Sun, N.; Zhu, Q.; Soomro, R. A.; Xu, B. Microcrystalline Hybridization Enhanced Coal-Based Carbon Anode for Advanced Sodium-Ion Batteries. *Advanced Science* **2022**, *9*, 2200023.

(23) Eckmann, A.; Felten, A.; Mishchenko, A.; Britnell, L.; Krupke, R.; Novoselov, K. S.; Casiraghi, C. Probing the Nature of Defects in Graphene by Raman Spectroscopy. *Nano Lett.* **2012**, *12* (8), 3925−3930.

(24) Tang, S.; Lu, G.; Su, Y.; Wang, G.; Li, X.; Zhang, G.; Wei, Y.; Zhang, Y. Raman Mapping of Lithiation Process on Graphene. *Acta Phys. -Chim. Sin.* **2022**, *38* (3), 2001007.

(25) Kelemen, S. R.; Afeworki, M.; Gorbaty, M. L.; Cohen, A. D. Characterization of Organically Bound Oxygen Forms in Lignites, Peats, and Pyrolyzed Peats by X-Ray Photoelectron Spectroscopy (XPS) and Solid-State 13C NMR Methods. *Energy Fuels* **2002**, *16* (6), 1450−1462.

(26) Chen, D.; Zhang, W.; Luo, K.; Song, Y.; Zhong, Y.; Liu, Y.; Wang, G.; Zhong, B.; Wu, Z.; Guo, X. Hard Carbon for Sodium Storage: Mechanism and Optimization Strategies toward Commercialization. *Energy Environ. Sci.* **2021**, *14* (4), 2244−2262.

(27) Harris, P. J. F. Engineering Carbon Materials with Electricity. *Carbon* **2017**, *122*, 504−513.

(28) Yao, Y.; Fu, K. K.; Zhu, S.; Dai, J.; Wang, Y.; Pastel, G.; Chen, Y.; Li, T.; Wang, C.; Li, T.; Hu, L. Carbon Welding by Ultrafast Joule Heating. *Nano Lett.* **2016**, *16* (11), 7282−7289.

(29) Hettler, S.; Sebastian, D.; Pelaez-Fernandez, M.; Benito, A. M.; Maser, W. K.; Arenal, R. In-Situ Reduction by Joule Heating and Measurement of Electrical Conductivity of Graphene Oxide in a Transmission Electron Microscope. *2D Mater.* **2021**, *8* (3), 031001.
(30) Huang, J. Y.; Chen, S.; Ren, Z. F.; Chen, G.; Dresselhaus, M. S. Real-Time Observation of Tubule Formation from Amorphous Carbon Nanowires under High-Bias Joule Heating. *Nano Lett.* **2006**, *6* (8), 1699−1705.
(31) Li, R.; Yang, B.; Hu, A.; Zhou, B.; Liu, M.; Yang, L.; Yan, Z.; Fan, Y.; Pan, Y.; Chen, J.; Li, T.; Li, K.; Liu, J.; Long, J. Heteroatom Screening and Microcrystal Regulation of Coal-Derived Hard Carbon Promises High-Performance Sodium-Ion Batteries. *Carbon* **2023**, *215*, 118489.
(32) Wang, K.; Qian, J.; Sun, F.; Tian, Z.; Gao, J.; Zhao, G. In-Situ Catalytic Conversion of Coal Pyrolysis Gas to Nanoporous Carbon Rods and Superior Sodium Ion Storage Performance. *Fuel* **2020**, *281*, 118782.
(33) Wang, H.; Shi, L.; Yang, Z.; Liu, J.; Xu, Y.; Song, M.; Jiang, J.; Zhuang, Q.; Chen, Y.; Ju, Z. Recycling of Waste Coal-Based Filter Materials into Carbon Anode Materials for Potassium and Sodium-Ion Batteries. *Mater. Today Sustain.* **2023**, *24*, 100578.
(34) Liu, R.; Li, Y.; Wang, C.; Xiao, N.; He, L.; Guo, H.; Wan, P.; Zhou, Y.; Qiu, J. Enhanced Electrochemical Performances of Coal Liquefaction Residue Derived Hard Carbon Coated by Graphene as Anode Materials for Sodium-Ion Batteries. *Fuel Process. Technol.* **2018**, *178*, 35−40.
(35) Tian, Q.-Q.; Li, X.-M.; Xie, L.-J.; Su, F.-Y.; Yi, Z.-L.; Dong, L.; Chen, C.-M. Insights into the Carbonization Mechanism of Bituminous Coal-Derived Carbon Materials for Lithium-Ion and Sodium-Ion Batteries. *New Carbon Mater.* **2023**, *38* (5), 939−953.
(36) Cheng, D.; Li, Z.; Zhang, M.; Duan, Z.; Wang, J.; Wang, C. Engineering Ultrathin Carbon Layer on Porous Hard Carbon Boosts Sodium Storage with High Initial Coulombic Efficiency. *ACS Nano* **2023**, *17* (19), 19063−19075.


https://doi.org/10.1021/acsaem.3c02975
*ACS Appl. Energy Mater.* XXXX, XXX, XXX−XXX